

To appear in *The Astrophysical Journal*, v. 474

A Composite HST Spectrum of Quasars¹

Wei Zheng, Gerard A. Kriss, Randal C. Telfer, John P. Grimes
and Arthur F. Davidsen

Center for Astrophysical Sciences, The Johns Hopkins University
Baltimore, MD 21218-2695

E-mail address: zheng,gak,telfer,grimes,afd@pha.jhu.edu

ABSTRACT

We construct a composite quasar spectrum from 284 HST FOS spectra of 101 quasars with redshifts $z > 0.33$. The spectrum covers the wavelengths between 350 Å and 3000 Å in the rest frame, with a peak S/N level of ~ 130 per Å at ~ 1200 Å. Since $\sim 90\%$ of the sample quasars have redshift $z < 1.5$, the spectrum is suitable for studying the wavelength region shortward of Ly α without large effects from intervening Ly α forest absorption. Data in the waveband between 350 Å and 600 Å are mainly from the spectra of $z > 1.5$ quasars, for which significant corrections for the accumulated Lyman-series line and continuum absorption have been applied.

There is a significant steepening of the continuum slope around 1050 Å. The continuum between 1050 Å and 2200 Å can be modeled as a power law $f_\nu \propto \nu^\alpha$ with $\alpha = -0.99 \pm 0.05$. For the full sample the power-law index in the extreme ultraviolet (EUV) between 350 Å and 1050 Å is $\alpha = -1.96 \pm 0.15$. For the radio-loud subsample (60 objects), the EUV spectral index is $\alpha \simeq -2.2$, while for the radio-quiet subsample (41 objects) it is $\alpha \simeq -1.8$. The continuum flux in the wavelengths near the Lyman limit shows a depression of $\sim 10\%$. The break in the power-law index and the slight depression of the continuum near the Lyman limit are features expected in Comptonized accretion-disk spectra. Comptonization produces a power-law tail in the wavelength band shortward of ~ 1000 Å and smears out the Lyman-limit edge of the intrinsic accretion-disk spectrum.

In the EUV waveband, we detect several possible emission features, including one around 690 Å that may be O III+N III produced by the Bowen fluorescence effect. Comparing our composite spectrum with one made at higher redshifts by Francis et al. (1991), we find that the equivalent widths of Ly α and high-ionization emission lines are larger in our sample, reflecting a known luminosity dependence. The equivalent

¹Based on observations with the NASA/ESA Hubble Space Telescope, obtained at the Space Telescope Science Institute, which is operated by the Association of Universities for Research in Astronomy, Inc., under NASA contract NAS5-26555.

widths of low-ionization lines do not exhibit such a dependence, suggesting that the quasar EUV continuum above ~ 50 eV is steeper at higher luminosity. Radio-quiet quasars appear to show a slightly harder continuum and lower ionization levels in their emission lines.

Subject headings: Spectrum: Ultraviolet — quasar

1. INTRODUCTION

Three decades after their first identification (Schmidt 1963) more than 7000 quasars have been found (Hewitt & Burbidge 1993). Quasar spectra play a key role in observational cosmology. Most of them have been obtained with ground-based telescopes using various techniques, including wide-field prism surveys and spectroscopy at very high resolution. Despite differences in detail between individual objects, quasar spectra bear a strong family resemblance, including features such as a non-thermal power-law continuum, a UV excess, and broad emission lines. One way to study the general properties of quasars is by co-adding the spectra of a number of quasars. The first composite spectrum included only 14 quasars (Baldwin 1977a), while the latest ones (Boyle 1990; Francis et al. 1991) were made from several hundred optical spectra. High S/N composite spectra serve as a good reference for the intrinsic continuum shape and emission lines of quasars in the wavelength region longward of 1200 Å (in the quasar rest frame, and the same hereafter unless stated otherwise). Ground-based telescopes cannot, however, reveal the far-UV spectral region below 1200 Å for quasars with $z < 2$.

Several space-borne telescopes have filled this observational gap and further extended the observations of quasars to the extreme-ultraviolet (EUV) region. As of 1995 December, the International Ultraviolet Explorer (IUE) database contains more than 1500 low-resolution ($R \approx 300$) spectra of 158 quasars. An extensive IUE-based study of the quasar continuum was carried out by O'Brien, Gondhalekar, & Wilson (1988, OGW hereafter). Using ~ 200 IUE spectra of 59 quasars plus some data from ground-based observations, they found a considerable and gradual steepening of the continuum toward shorter wavelengths. The power-law index increases by ~ 1 from 1 μ m to ~ 800 Å. They derived an average power-law index ($F_\nu \propto \nu^\alpha$) of $\alpha = -0.67$ between 1216 Å and 1900 Å and $\alpha = -2.36$ between 800 Å and 1216 Å.

The Hubble Space Telescope (HST) has greatly extended our probe of the distant universe. The HST Faint Object Spectrograph (FOS) database is superior to the IUE database in terms of S/N level and spectral resolution (typically $R \approx 1500$). More than 800 FOS spectra of 246 quasars have been archived as of the end of 1995. The average redshift of quasars in the FOS database is significantly higher than in the IUE database. The spectral properties of some low-redshift quasars have been reported as part of the HST Key Project “Quasar Absorption Lines” (Bahcall

et al. 1993; Laor et al. 1994, 1995). We therefore focused on the FOS archival data for quasars of higher redshift, in an attempt to study the sub–Ly α region in quasar spectra. We have constructed a composite spectrum of quasars, based on 284 FOS spectra of 101 quasars. It covers a range between 350 Å and 3000 Å and reveals some features which are not seen in individual spectra. In particular, we find that the far–UV continuum slope is significantly different above and below ~ 1000 Å.

2. DATA REDUCTION

Archival FOS spectra were retrieved from the Space Telescope Science Institute in the form of calibrated data. The selection criteria were (1) target redshift $z > 0.33$; and (2) no obvious broad absorption lines. The low–redshift limit was set so that the intrinsic spectral region shortward of 912 Å is accessible with HST. Our sample includes 55 spectra with grating G160L, 29 with G130H, 93 with G190H, 90 with G270H, and 17 with G400H. The G160L and G130H spectra were checked for proper background subtraction and reprocessed if necessary. We measured the average count level at the wavelengths below 1150 Å where the instrumental sensitivity should be zero, and used it to correct the background subtraction. The distribution of the sample with redshift is displayed in Fig. 1. About 90% of our sample have $z < 1.5$. In this redshift range, the correction for Ly α forest–line absorption is small ($\lesssim 0.1$). Despite their small number, the spectra of $z > 1.5$ quasars are important as they reveal the waveband shortward of 600 Å. In these quasars, numerous Ly α –forest and metal absorption lines significantly alter the intrinsic spectra.

The selected FOS spectra were corrected for Galactic extinction. The hydrogen column density toward each quasar was estimated using the task `colden` of the Einstein On–Line Service, Smithsonian Astrophysical Observatory, which is based on the work of Stark et al. (1992). For several southern objects, the column densities were interpolated from the results of Heiles & Cleary (1979). The E_{B-V} values were calculated using the formulation of Burstein & Heiles (1978). We used the Seaton curve (Seaton 1979) to correct for extinction. The spectra were then shifted to the objects’ rest frame. Data points in the windows near the significant airglow lines at 1216 Å and 1304 Å in the observer’s frame were replaced by values linearly interpolated from neighboring parts of the spectrum. If a spectrum contained an obvious flux discontinuity due to absorption by an external Lyman–limit system, only the undepressed portion of the spectrum was used. Every spectrum has been visually checked for cosmic–ray spikes, damped Ly α absorption lines, or densely clustered absorption lines. The data points affected by these abnormal features were not used in the combining process.

In the quasar rest frame, each spectrum was resampled with 0.1 Å bins, roughly corresponding to the rest–frame bin size of the original G130H pixels in the highest redshift quasars. If a new bin is entirely inside an old bin, the flux of the new bin is taken from the old one. However, if the new

bin overlaps two of the old bins, then the flux is taken as the weighted mean of the fluxes from the two old bins. The error was treated in the same way, along with two additional factors: (1) the weighted mean was calculated using the weighting $1/e^2$, where e is the error, and (2) the error was multiplied by $\sqrt{p/0.1(1+z)}$ where p is the original data pixel in units of Å. While this propagates the magnitude of errors correctly, the rebinning process does introduce correlated errors between adjacent pixels that we do not track.

The EUV continuum of high-redshift quasars is unavoidably depressed by the Lyman-line absorption and the Lyman continuum absorption of intervening clouds. The accumulated absorption produces a trough centered around 700 Å, commonly referred to as the Lyman valley (Møller & Jakobsen 1990). The exact shape of the Lyman valley depends on the number of absorption lines and their distribution. We generated correction curves using the empirical formula for the forest-line distribution, i.e.

$$\frac{\partial^2 n}{\partial z \partial N} = A(1+z)^\gamma N^{-\beta} \quad (1)$$

(Press & Rybicki 1993). For $z > 2$ we chose $\beta = 1.5$, $A = 2.3 \times 10^7$ and $\gamma = 2.46$ because, with these parameter values, we were able to produce a line number comparable to that in the recently published data for high-redshift quasars (Hu et al. 1995). At lower redshifts ($z \approx 0.5$), Kulkarni & Fall (1993) found $\beta = 1.48$, $A = 5.5 \times 10^7$ and $\gamma = 0.21$. Since these two sets of parameters yield a negligible difference in the average opacity at low redshifts, we used only the parameters derived at $z > 2$.

Using the formulation for the average line-absorption opacity

$$\tau(z) = \frac{dn}{dz} \frac{< W_\lambda >}{\lambda} (1+z), \quad (2)$$

where dn/dz is the number of lines per unit redshift and $< W_\lambda >$ is the mean rest-frame equivalent width of Ly α lines averaged over the assumed distribution in column density (Møller & Jakobsen 1990), we calculated the wavelength-averaged opacity produced by Lyman-series lines up to level 50. The accumulated Lyman-continuum absorption was calculated using $\tau(\lambda) = N\sigma_0 (\lambda/\lambda_0)^3$, where N is the neutral hydrogen column density and σ_0 is the hydrogen photoionization cross section at the Lyman-limit wavelength λ_0 . We produced a set of correction curves at different redshifts for lines with column density between 2×10^{12} and 10^{16} cm $^{-2}$. The low limit was set by the recent Keck spectroscopic observations (Hu et al. 1995). Absorption by any cloud with column density greater than 10^{16} cm $^{-2}$ produces a noticeable Lyman-limit edge in a spectrum, and its correction is straightforward. Fig. 2 displays correction curves at different redshifts and clearly shows that the correction is small ($\lesssim 0.1$) for $z < 1.5$. We first applied a general correction for every merging spectrum. For quasars with $z > 1.5$, if the absorbers with column density $N > 10^{16}$ cm $^{-2}$ are known in the literature, we applied additional corrections for them.

To merge the quasar spectra we used a technique similar to that described by Francis et al. (1991). We sorted the quasar spectra by their wavelength coverages. Starting from the quasar

spectrum that covers the longest wavelengths, we normalized the flux of the second spectrum to the first so that the average flux of the two spectra matched each other in the overlapping region. To assure that the normalization applied to the continuum only, wavelength windows surrounding major emission lines were excluded. Using this new summed spectrum, the next spectrum was normalized and merged. This process was repeated to include more spectra, until the spectrum that covers the shortest wavelengths was included. We also practiced this method starting at the shortest wavelength end and found that the overall continuum and emission-line features were virtually identical. However, the summation from longer wavelengths is preferred, as it follows the direction from high to low S/N level at shorter wavelengths.

Throughout the combining process the weighted mean and the error in the weighted mean were calculated at each 0.1 \AA pixel. We tried a weight $w = f/e^2$, where f is the flux and e the error. With such a weighting a flux spectrum would be converted into an approximate count spectrum. Such a summation resembled the addition of raw count spectra and produced an output with the highest possible S/N level (with a peak value of ~ 300 per \AA). However, a small number of high-quality spectra were given particularly high weights so that the final spectrum bears the signature of strong absorption lines in these few quasars. We have, therefore, chosen a uniform weight in order to produce a smoother spectrum, particularly at shorter wavelengths, more representative of the overall quasar population. For every data point of every merged spectrum, the average S/N level was calculated over 10 points (1.0 \AA) on either side. If the average S/N level per pixel was below 0.3 this data point was excluded.

Using this composite spectrum as a template, we further applied a renormalization process. All the spectra were normalized so that the average flux level in individual spectra, excluding the wavelength windows surrounding major emission lines and the data points with average S/N level less than 0.3, matched that of the template spectrum in the corresponding wavelength range. The sum of the normalized spectra was smoother than the template at shorter wavelengths where the S/N level was lower, and it serves as the final composite spectrum.

Fig. 3 displays the number of merged spectra as a function of wavelength. For some objects, multiple observations taken with the same grating exist. In such cases, we merged these spectra into a single spectrum, which counts as one in Fig. 3. Near 1200 \AA the number of merged spectra reaches a peak of ~ 100 , and at very short wavelengths it is only 2 or 3. Fig. 4 displays the S/N level of the composite spectrum after binning by 10 pixels. The spectral region near 1200 \AA has the highest S/N level of ~ 130 per \AA , and the region near 350 \AA has $\text{S/N} \approx 8$ per \AA . The actual S/N level may be slightly lower as the flat field correction of the FOS instrument limits the S/N in any given spectrum to ~ 50 or less. But we do not expect a significant effect as any flat-field irregularities should be smeared out due to the different redshifts.

3. RESULTS

3.1. Continuum

The composite HST quasar spectrum, as shown in Fig. 5, shows a change in slope of the continuum between 350 Å and 3000 Å that can be approximated as a broken power law. We used the IRAF task `specfit` (Kriss 1994) to fit the shape of the continuum and the emission lines. With `specfit`, complex line and continuum models can be fitted to data using a nonlinear χ^2 -minimization technique. For our fits we binned the composite spectrum by three pixels (0.3 Å). The following wavelength windows for the continuum fitting were selected: 350–450, 500–640, 720–750, 800–825, 930–950, 1100–1130, 1450–1470, 1975–2010, 2150–2200 Å. Above 900 Å any small deviations from a power law that are due to weak emission features, Fe II in particular, yield significant $\Delta\chi^2$ because of the very high S/N level. Therefore, the selected windows at long wavelengths are narrow. The region near 912 Å was excluded because of an apparent local depression in flux (discussed below). The region longward of 2200 Å was not fitted because of the strong Fe II emission seen there.

Since the propagated error arrays in our calculations contain correlated errors that are not taken into account, we experimented with two different methods of assigning errors and evaluating the goodness of our fits. The first directly uses the propagated error array. The second uses the root-mean-square (rms) spectrum. An advantage of using the rms spectrum for the error bars is that it avoids giving excessive weight to the longer-wavelength portions of the spectrum where the number of merging spectra is large. To calculate the rms spectrum, each normalized spectrum was differenced with respect to the composite. The squared differences were summed, with equal weights, and the sum was divided by the number of spectra contributing to each pixel. The square root of the result gives the rms deviation, shown in Fig. 6. The dispersion is $\sim 10\%$ around 2500 Å, and $\sim 30\%$ around 400 Å.

A fit with a single power law continuum using the propagated error array yields $\chi^2 = 13,684$ for 1504 data points and 2 free parameters. In contrast, a broken power law gives $\chi^2 = 1196$ for 1504 points and 4 free parameters, with the power-law index $\alpha = -1.00 \pm 0.01$ above 1038 Å and $\alpha = -2.02 \pm 0.02$ below. We conclude that a broken power law is a good fit to the continuum (except for the region between 900 Å and 1200 Å where the continuum shape changes gradually), and a single power law can be excluded at much greater than the 5σ confidence level.

Fits using the rms spectrum for the errors give similar results. The fitted power-law index $\alpha = -0.99 \pm 0.01$ above ~ 1052 Å and $\alpha = -1.96 \pm 0.02$ below. The power-law index in the region with $\lambda > 1052$ Å derived with the rms array is the same as that with the propagated error array, and it is slightly different for $\lambda < 1052$ Å. Therefore the power-law indices in Table 1 are not affected significantly by the use of different error arrays, and we feel that using the rms array may yield more representative results at shorter wavelengths. Note that the 1σ errors only reflect the formal estimates of the fitting process, and the actual errors are somewhat higher because of the uncertainties introduced in the merging process.

The break point of the power law is 1052 ± 13 Å. This value is sensitive to the fitting windows chosen at shorter wavelengths, and may vary by ~ 50 Å. The continuum fit parameters are summarized in Table 1. Separate fits were also performed for radio-loud and radio-quiet quasars, and these results are also given in Table 1 and discussed below. As one can see in Fig. 5, one power law can describe well the wavelengths between 1300 Å and 3000 Å, despite the presence of Fe II emission.

The spectral region near the Lyman limit is of special interest. We plot this region in Fig. 7 with a pixel size of 0.3 Å. With respect to the fitted broken power-law continuum, there is a $\sim 10\%$ trough just below the Lyman limit. The trough is a smooth feature centered around 870 Å, with a wavelength span of ≈ 70 Å. It does not seem to arise from associated absorbers because it recovers much faster at shorter wavelengths than a $\tau \propto (\lambda/\lambda_0)^3$ law predicts. If included in the fit, this trough contributes substantially to χ^2 as shown in the lower panel of Fig. 7. Our fits to a Comptonized accretion disk spectrum, discussed in §4.4, address the statistical significance of the trough in more detail. Such a trough is seen in the merged spectra made of several subsamples and therefore is not an artifact due to a few individual quasars. There are several spectra that show significant broad absorption features near the Lyman limit, and they will be discussed in a separate paper (Zheng et al. 1996).

3.2. Emission Lines

We used multiple Gaussian components to fit the emission lines using `specfit`. Ly α , C IV, O VI, N V and Mg II were fitted with two Gaussians: a narrow component and a broad one. The line widths of the two N V components were tied to the respective Ly α components, and the N V/Ly α wavelength ratio was fixed at its rest-frame value. Other lines were modeled with one Gaussian. The line widths of Al III, Si III] and C III] were tied together in the fitting process. The fitting results are listed in Table 2. The flux units are arbitrary on a relative scale with $I(\text{Ly}\alpha) = 100$. In addition to the major emission features marked in Fig. 5, some weak features, such as C III $\lambda 977$ and N III $\lambda 991$, can be identified because of the high S/N level. The emission feature around 780 Å has been identified as Ne VIII (Hamann, Zuo, & Tytler 1995). The ionization level of Ne VIII (206 eV) is extremely high. If the line emission is generated by collisional excitation, a high temperature ($T > 5 \times 10^4$ K) is needed in the region in which these lines are formed as their excitation energies are greater than 12 eV. The Ne VIII profile, with a FWHM ≈ 12000 km s $^{-1}$, is much broader than that of most other lines, and O VI emission also exhibits a broad base of similar width. The emission feature around 690 Å may be O III+N III arising from the Bowen fluorescence effect (Eastman & MacAlpine 1985; Netzer, Elitzur, & Ferland 1985). The O $^{++}$ and N $^{++}$ ions have transitions whose wavelengths coincide very closely with He II $\lambda 304$ Å, which was recently detected in a high- z quasar (Davidsen, Kriss, & Zheng 1996a). Abundant He II Ly α photons in the line-emitting region can excite the O $^{++}$ and N $^{++}$ ions and produce cascade transitions. Theoretical estimates suggest that

the O III/He II Ly α intensity ratio is on the order of 0.1 and is only weakly dependent on the ionizing flux. This feature is not present in every spectrum that covers the wavelengths between 650 Å and 700 Å, so its identification is only suggestive. There is also an emission feature near 833 Å. We tentatively identify it as O II λ 833.80, while an alternative identification as O III λ 833.97 is also possible. At wavelengths shorter than 600 Å we did not attempt to identify emission features because of the limited S/N level.

4. DISCUSSION

4.1. EUV Continuum Shape

The continuum shape above 600 Å can be determined quite accurately, because the spectrum is composed of mainly $z < 1.5$ quasars and the Lyman–valley correction is small. Below 600 Å, the merged spectra are mainly derived from $z > 1.5$ quasars, and the results depend more and more on the correction as the redshift increases. The correction curves applied are based on Equation (1), which is statistical in nature. Our Monte–Carlo simulations of forest–line absorption (with column density $N < 10^{16} \text{ cm}^{-2}$) suggest fluctuations of $\sim 10\%$ in the average decrements. We find that the actual average line opacity, due to line blending, is $\sim 15\%$ smaller (for $z \sim 3$) than Equation (2) indicates. As lines with higher column density contribute more significantly in the wavelengths around 700 Å, the correction for lines between 10^{16} and 10^{17} cm^{-2} introduces larger errors. Our calculations show that, at $z \sim 2$, absorption lines with $10^{16} < N < 10^{17} \text{ cm}^{-2}$ may affect the decrement at 350 Å and lead to an uncertainty in the power–law index between 350 Å and 1050 Å of ~ 0.15 . However, such a large error is unlikely because an absorption line with $N \geq 10^{16} \text{ cm}^{-2}$ should produce a visible Lyman–limit edge, and our selection process has carefully excluded the wavelength regions shortward of such visible edges. Combining all these facts together, we feel that an uncertainty of 0.15 in the power–law index may be a reasonable estimate between 350 Å and 1050 Å. At wavelengths above 1050 Å, a comparison between different quasar subsamples yields a dispersion in α of ~ 0.05 .

Our measurements of the quasar continuum can be compared with earlier IUE results. OGW (1988) found the continuum steepening toward shorter wavelengths. Excluding blazars and broad–absorption–line quasars, their power–law indices are $\alpha = -0.67 \pm 0.05$ for $\lambda > 1216 \text{ Å}$, -2.14 ± 0.13 for $1216 > \lambda > 912 \text{ Å}$, and -2.36 ± 0.21 for $1216 > \lambda > 800 \text{ Å}$. The far–UV power–law index they derived is somewhat steeper than our result of $\alpha \approx -2.0$. Their subsample with $z > 1.1$ yielded even steeper values at shorter wavelengths, i.e. $\alpha = -0.46 \pm 0.05$ for $\lambda > 1216 \text{ Å}$, -2.57 ± 0.15 for $1216 > \lambda > 912 \text{ Å}$, and -2.86 ± 0.24 for $1216 > \lambda > 800 \text{ Å}$. The OGW results are in qualitative agreement with ours, but our larger sample and more sensitive HST observations more accurately determine the power–law index. OGW (1988) suggested that the steepening is gradual from the

optical to the UV. We find that the continuum between ~ 1200 Å and 3000 Å can be approximated with one power law.

At shorter wavelengths, O'Brien (1987) used the IUE spectra of three radio-quiet quasars to derive a mean power-law index of $\alpha = -1.77 \pm 0.46$ between 600 Å and 912 Å. Our more precise measurement, while consistent with his result, suggests that for our total sample the quasar continuum in this spectral region is actually slightly steeper. For our radio-quiet subsample, however, we find α very similar to O'Brien's value, but with a considerably smaller uncertainty.

EUV photons play important roles in many physical processes, and knowledge of the quasar EUV continuum shape would lead to improvements in many theoretical models. Emission lines in active galaxies and quasars are believed to be powered by photoionization. Models with various EUV continuum shapes yield different line intensities (Krolik & Kallman 1988). A typical AGN power-law index adopted for the EUV band is $\alpha \approx -1.0$ (Mathews & Ferland 1987) which predicts too strong an ionizing continuum compared to our result of $\alpha \approx -2.0$. Our composite spectrum, with a power-law extrapolation into the soft-X-ray band, can serve as a reasonable input for photoionization models in the study of AGN.

Quasar radiation plays a key role in the reionization of the intergalactic medium in the early universe (e.g., Shapiro, Giroux, & Babul 1994). The exact quasar continuum shape (Miralda-Escude & Ostriker 1990) may dictate the He II-ionizing metagalactic radiation field, which in turn affects the He II opacity in the intergalactic medium. The recent measurement of the He II opacity (Davidsen et al. 1996a) in the intergalactic medium is compatible with a background radiation field with $\alpha \approx -1.8$ (Davidsen et al. 1996b). This is very similar to the value found here for radio-quiet quasars, which should dominate the metagalactic background radiation. The continuum shape of quasars also affects their detectability at high redshifts. An order of magnitude fewer quasars are predicted to be observable in the UV band if their EUV continuum power law index is $\alpha = -2$ compared with $\alpha = -1$ (Pickard & Jakobsen 1993).

4.2. Relation with Radio Properties

We divided our sample into radio-loud and radio-quiet objects and applied the same fitting process to the lines and the continuum. Radio-loud quasars are defined as those with the logarithm of the ratio of the 6cm flux to the flux in the optical B band $R_L = \log(f_{6cm}/f_B) > 1$. To evaluate R , we used fluxes for the selected quasars from Véron-Cetty & Véron (1993). The composite spectra of radio-loud and radio-quiet quasars are compared in Fig. 8. Both composite spectra cover a similar wavelength range and exhibit similar spectral properties. At very short wavelengths the composite spectrum of radio-loud quasars is entirely due to two objects: Q0446-2049 between approximately 475 Å and 600 Å, and OQ 172 below 475 Å, so the result is quite uncertain at these wavelengths.

For radio-loud quasars, the fitted power-law index $\alpha = -1.02 \pm 0.01$ above 1050 Å and

-2.16 ± 0.03 below. For radio-quiet quasars, it is -0.86 ± 0.01 and -1.77 ± 0.03 , respectively. Our results are in agreement with Christiani & Vio (1990) in terms of the similar continuum shape between 1000 Å and 3000 Å for their subsamples of radio-selected and optically-selected quasars. Below 1000 Å, the continuum of radio-loud quasars appears to be steeper than that of radio-quiet quasars. Such a difference was also noticed by OGW (1988) in their radio-selected and optically-or-X-ray selected samples.

For radio-quiet quasars, the Mg II intensity is stronger, and the intensities of C IV and O VI are weaker. Radio-quiet and radio-loud quasars therefore appear to show somewhat different ionization levels of their emission lines. To check whether this is a luminosity effect, we compared the mean redshift of the subsamples. As shown in Table 1, these two groups of quasars have similar mean redshifts. We also calculated the quasar specific luminosity at 1000 Å, assuming $H_0 = 75 \text{ km s}^{-1} \text{ Mpc}^{-1}$ and $q_0 = 0.5$. If a spectrum does not cover 1000 Å, the flux was extrapolated from that at the wavelengths closest to 1000 Å, using the power law derived from the whole sample (Table 1). The mean luminosities of the radio-loud and radio-quiet quasars are both $2.4 \times 10^{30} \text{ erg s}^{-1} \text{ Hz}^{-1}$. We therefore conclude that the differences seen are not due to a luminosity effect.

4.3. Redshift and Luminosity Effects

Fig. 9 plots our composite spectrum for radio-quiet quasars and the spectrum of Francis et al. in the region of overlap. At wavelengths longer than 1000 Å, our spectrum is mainly derived from quasars with $z < 1.5$, while that of Francis et al. is mainly for $z > 2.5$. The two spectra are normalized so that the continuum levels around 1450 Å match each other. The high- z spectrum shows a significant flux depression shortward of Ly α resulting from Ly α forest-line absorption. The average power-law index between 1200 Å and 2200 Å is ~ -0.8 , reflecting a harder UV continuum at higher redshifts. The difference in the continuum shape does not occur smoothly. The continuum in the two spectra matches fairly well between 1200 Å and 1900 Å. Above 1900 Å the continuum in the high- z spectrum becomes significantly harder ($\alpha = -0.32 \pm 0.05$). This result supports the finding of OGW (1988) that quasars of higher redshift show harder UV continua. Francis (1993) further confirmed that the effect is a correlation with redshift and not with luminosity.

By comparing the two composite spectra in Fig. 9 one can also see that the intensities of several high-ionization emission lines are different. One should approach these differences cautiously, however, since our composite spectrum is more subject to selection effects and more heterogeneous than the Francis et al. spectrum. The equivalent widths of Ly α , C IV, He II+O III], and O VI decrease by approximately 39%, 37%, 42%, and 56%, respectively, from $z \sim 1$ to $z \sim 3$. In particular, the O VI intensity is significantly weaker at higher redshifts, but we note that for Ly α and O VI, the Francis et al. spectrum is strongly affected by Ly α forest-line absorption. On the

other hand, the equivalent widths of low-ionization lines, such as Mg II, C III], O I and Si IV remain basically unchanged. The trend that Ly α and high-ionization lines exhibit significant decreases toward higher redshifts (and, consequently, higher luminosities: the Baldwin effect, Baldwin 1977b) supports the hypothesis that the Baldwin effect is due to a luminosity dependence of the shape of the ionizing continuum (Zheng, Fang, & Binette 1992), i.e. the continuum shape above ~ 50 eV may be steeper at higher luminosities.

4.4. Comptonized Disk Spectrum

The flux discontinuity at the Lyman limit of 912 Å is a critical test of the nature of the UV excess in AGN. The rising continuum in the optical–UV band resembles the thermal spectrum of an accretion disk (Shields 1978; Malkan & Sargent 1982). Such a disk, with a characteristic temperature of $\sim 10^4$ K, should produce a significant absorption edge at the Lyman limit (Kolykhalov & Sunyaev 1984). Previous searches for such a feature in the optical and IUE database have yielded negative results (Antonucci, Kinney, & Ford 1989; Koratkar, Kinney, & Bohlin 1992; Koratkar et al. 1995). In general these observations limit any discontinuity due to a Lyman–edge feature to less than 15%.

Previous investigations of Lyman–limit discontinuities in quasar spectra based on HST data have led to different, tentative reports. Sun, Malkan, & Chang (1993), analyzing the FOS spectra of 21 quasars, suggested that $\sim 24\%$ of the sample have possible rest–frame Lyman–limit absorption edges. They found similar results for a sample of medium– to high–redshift quasars using optical spectra obtained at Lick Observatory and at the Hale Observatory. On the other hand, Tytler & Davis (1993) found no discontinuity across the Lyman limit in the FOS spectra of 27 quasars. While it is not clear whether these two conflicting reports are based on different samples, the larger size of the sample comprising our mean spectrum assures higher quality statistics for examining the Lyman–limit region.

Two features in the mean spectrum we have constructed suggest association with an intrinsic spectral feature in the Lyman–limit region. The first is the sharp break in the continuum spectral index. The second is the slight depression in the continuum flux shortward of the Lyman limit noted in §3.1. The continuum break resembles that observed shortward of 1000 Å in the Hopkins Ultraviolet Telescope spectrum of the quasar 3C 273 (Davidsen et al. 1996c). The change in the spectral index is so abrupt that it cannot be produced either by reddening or by intervening absorption, including the Lyman–series lines and the Lyman continuum (which we have largely corrected for). Comptonization of an accretion–disk spectrum with an intrinsic Lyman edge can produce a continuum shape very similar to what is shown by our mean spectrum in Fig. 5. It produces a power–law high–energy tail and smears out any intrinsic Lyman–limit discontinuity (Czerny & Zbyszewska 1991). The emergent spectrum still bears the signature of a Lyman edge, however, if the optical depth to scattering is not too high.

To fit the overall continuum shape of our mean quasar spectrum, we computed an intrinsic disk spectrum in the Schwarzschild metric that was a sum of blackbodies with an empirical Lyman limit feature as described by Lee, Kriss, & Davidsen (1992). A spherical corona with optical depth $\tau_e = 1.0$ to Compton scattering was assumed to surround the disk. The Comptonized disk spectrum was calculated using the formulation of Czerny & Zbyszewska (1991) as described by Lee et al. (1992). The shape of the intrinsic disk spectrum is invariant for a fixed ratio \dot{m}/M_{BH}^2 , and the spectral index of the Comptonized high energy tail depends almost entirely on the Compton y parameter $y \propto \tau_e^2 T_c$ (Lee 1995). The mass accretion rate determines the total luminosity, and this we normalized to the mean luminosity of the quasar sample. The location of the Lyman-edge depends largely on the disk inclination, i . Thus the free parameters in the fit were the mass of the central black hole, M_{BH} , the mass accretion rate, \dot{m} , the temperature of the Comptonizing medium, T_c , the optical depth of the empirical Lyman edge, τ_{Ly} , and the inclination of the disk normal to the line of sight, i .

Our fits used the same continuum windows listed in §3.1 for the broken power-law continuum fits except that we also included the Lyman edge region from 825–930 Å that was excluded in those previous fits. For error bars we used the propagated errors computed in the merging process. We find that the best fit requires a Lyman edge of modest optical depth in the emergent disk spectrum. The best fit has a Lyman limit optical depth of $\tau_{Ly} = 0.8$ and yields $\chi^2 = 1715$ for 1853 points and 5 free parameters. $\tau_{Ly} = 0.0$ results in a fit with $\chi^2 = 1761$, and this can be excluded at $> 5\sigma$ confidence relative to the fit with a Lyman edge of finite optical depth.

Fig. 10 shows the best-fit Comptonized accretion-disk spectrum compared to the 1-Å resolution mean quasar spectrum. This model has $M_{BH} = 1.4 \times 10^9 M_\odot$, $\dot{m} = 2.8 M_\odot \text{ yr}^{-1}$, $\tau_{Ly} = 0.8$, $i = 30^\circ$, and $T_c = 4.1 \times 10^8 \text{ K}$. For a Schwarzschild black hole the total luminosity of the disk is $8.5 \times 10^{45} \text{ erg s}^{-1}$, which is 5% of the Eddington limit for a $1.4 \times 10^9 M_\odot$ black hole.

Although an inclination closer to 60° would have been expected for a sample of randomly oriented disks, we note that the heterogeneous HST archive sample is unlikely to be random. Our exclusion of BAL QSOs is likely to avoid disks at high inclinations. The large fraction of radio-loud objects in the sample will also produce a bias towards low inclinations.

The geometrically thin, optically thick “standard” accretion disk model has been criticized on many counts (e.g., Antonucci 1988, 1992). Among its shortcomings are the lack of strong Lyman–edge features in the observations, the difficulty of constructing disks with hot–enough tails to match the observed soft–X–ray excesses of AGN, and observed polarization properties that are inconsistent with simple predictions. Comptonization of the intrinsic disk spectrum in a quasi–spherical scatterer resolves many of these problems.

As noted by Czerny & Zbyszewska (1991), Comptonization can broaden an intrinsic Lyman edge and decrease its contrast to the point where a broad range of intrinsic disk parameters produce similar emergent spectra. The ability of such a model to match the weak Lyman limit feature in our mean spectrum is illustrated by our fit in Fig. 10.

O’Brien (1987) showed that an extrapolation of a ν^{-2} power law may connect the UV intensity to the soft-X-ray flux level around 0.3 keV in many quasars. This implies that, if the EUV continuum in our composite spectrum is representative, a single power law representing the high energy tail of a Comptonized accretion-disk spectrum may bridge the gap between the far-UV and the soft-X-ray bands. A Comptonized accretion disk fit to the Hopkins Ultraviolet Telescope (HUT) spectrum of Mrk 335 (Zheng et al. 1995) matches both the far-UV spectral shape in the Lyman-limit region and the soft-X-ray excess observed with the Broad Band X-ray Telescope (Turner et al. 1993).

If the Comptonizing medium has a largely spherical distribution, this can resolve many of the problems that recent polarization observations present for the thin disk model. Simple disk models show a low polarization increasing to the blue with a large drop beyond the Lyman limit due to the large absorption opacity of the Lyman continuum (Laor, Netzer, & Piran 1990). This predicted behavior is not observed in recent observations (Impey et al. 1995; Koratkar et al. 1995; Antonucci et al. 1996) which generally show little or no polarization and occasionally a *rise* beyond the Lyman limit rather than a drop. Moreover, the polarization vectors tend to be parallel to the radio-jet axis rather than perpendicular as one would expect if the jet were oriented perpendicular to the disk. A more physically realistic treatment of the polarized radiative transfer in a thin disk atmosphere (Blaes & Agol 1996) demonstrates that polarization can increase across the Lyman limit as observed. If most of the intrinsic disk radiation is Compton scattered, however, the polarization properties will be determined by the Compton scattering medium, not the disk atmosphere. If the scatterer is spherical, the polarization will be low. Antonucci et al. (1996) note that the polarization vector will lie parallel to the radio jet if the scatterer is slightly extended along the radio axis. This is perhaps not unexpected if a wind from the disk feeds the scattering region.

Although strong Comptonization can obscure many of the intrinsic properties of the disk spectrum, it does not destroy them. The shape of the spectrum near the peak in νf_ν and to the red is still determined predominantly by the black hole mass and the accretion rate. The position of any surviving Lyman-edge feature depends on the disk inclination. The spectral index of the high energy tail is diagnostic of the optical depth and temperature in the Comptonizing medium. Given the strong suggestion that Comptonization dominates the appearance of our composite HST spectrum, future disk models should take this feature explicitly into account.

5. SUMMARY

We have constructed a composite spectrum from 284 HST/FOS spectra of 101 quasars with $z > 0.33$. The UV continuum in the composite quasar spectrum can be fitted with a broken power law with a break around 1050 Å. At longer wavelengths the power-law index is $\alpha \simeq -1.0$. The

EUV continuum can be fitted with a power law of $\alpha \simeq -2.0$ without a noticeable turnover toward higher frequencies. Near the Lyman limit the continuum flux is depressed by $\sim 10\%$ relative to surrounding wavelengths. These features match the characteristics of thermal emission from an accretion disk with Lyman–edge absorption that is modified by electron scattering, suggesting that the UV bump may be produced by a Comptonized accretion–disk spectrum.

The strengths of high-ionization emission lines show a significant luminosity dependence, probably due to evolution of the UV continuum shape. In contrast, the equivalent widths of low-ionization lines do not exhibit such a dependence, suggesting that the continuum evolution may take place mainly in the energy band above 50 eV. The EUV continuum appears to be steeper in radio–loud quasars ($\alpha \simeq -2.2$) than it is in radio–quiet quasars ($\alpha \simeq -1.7$). Radio–quiet quasars appear to show slightly lower ionization levels in their emission lines.

The accumulated quasar radiation, with a continuum spectrum as found here, is capable of ionizing helium in the intergalactic medium and producing an opacity comparable to that recently measured with HUT (Davidsen et al. 1996a). Our findings support models that attribute metagalactic radiation in the early universe to quasar radiation.

Support for this work has been provided by contract NAS5–27000 and grant NAG5–1630 from NASA, and grant AR–4389.01–92A and AR–5284.01–93A from the Space Telescope Science Institute, which is operated by the Association of Universities for Research in Astronomy, Inc., under NASA contract NAS5–26555. We thank P. Hewett for providing the ground–based composite spectrum of Francis et al. (1991) in digital form.

Table 1. Fitted Power-Law Index^a

Sample	All Quasars	Radio Loud	Radio Quiet
Number of Objects	101	60	41
Mean Redshift	0.93	0.87	0.95
Wavelength Range (Å)			
1050–2200	-0.99 ± 0.01	-1.02 ± 0.01	-0.86 ± 0.01
600–1050	-2.02 ± 0.05	-2.45 ± 0.05	-1.83 ± 0.03
350–1050	-1.96 ± 0.02	-2.16 ± 0.03	-1.77 ± 0.03

^a The 1σ errors are statistical only, obtained from the error matrix of the fit. Due to the smaller sample size and the Lyman-valley correction, the actual errors below 1050 Å are probably on the order of ± 0.15 .

Table 2. Emission Line Strengths in Composite Quasar Spectrum

Line	λ_0 (Å)	Whole Sample		Radio Loud		Radio Quiet	
		Flux	EW (Å)	Flux	EW (Å)	Flux	EW (Å)
O III + N III ^a	~ 690	4.6 ± 1.6	3.6	5.2	4	5.1	3.5
Ne VIII	773.71	4.0 ± 1.5	3.2	3.6	3	4.2	4
O II ^a	833.80	1.4 ± 0.3	1.2	0.5	0.4	2.2	1.6
C III	977.02	0.9 ± 0.3	0.7	0.8	0.6	1.4	1.1
N III	990.98	1.1 ± 0.4	0.8	0.8	0.6	1.2	1.1
Ly β + O VI	~ 1031	19 ± 2	16	19	17	16	12
Ar I ^a	1066.66	0.6 ± 0.2	0.5	0.5	0.4	1.3	1.0
Ly α	1215.67	100	92	100	96	100	85
N V	1240.15	11 ± 1	10	10	10	14	10
O I	1303.94	1.3 ± 0.2	1.2	1.3	1.2	1.1	1.0
C II	1334.53	0.3 ± 0.1	0.3	0.2	0.2	0.4	0.4
Si IV + O IV]	~ 1400	7.5 ± 0.5	8	6.8	8	8.1	8
C IV	1549.01	62 ± 0.4	69	66	77	52	59
He II	1640.46	3.9 ± 0.2	4.5	4.3	5	3.4	3.9
O III]	1664.15	2.9 ± 0.3	3.4	3.2	3.7	2.7	3.1
N III]	1750.46	0.5 ± 0.1	0.7	0.7	0.9	0.2	0.2
Al III	1857.40	2.4 ± 0.3	3.5	2.3	3.6	2.9	3.5
Si III]	1892.03	2.4 ± 0.3	3.5	2.3	3.5	2.8	3.5
C III]	1908.73	11.5 ± 0.3	17	11	17	12	17
C II]	2324.27	2.9 ± 0.9	5	2.9	6	2.3	4
Fe II	~ 2400	18 ± 2	37	20	38	12	22
Mg II	2798.74	25 ± 1	50	24	50	33 ^b	64

^a Tentative identifications.

^b Profile incomplete.

REFERENCES

Antonucci, R. 1988, in *Supermassive Black Holes*, ed. M. Kafatos (Cambridge: Cambridge University Press), 26

_____. 1992, in *Testing the AGN Paradigm*, ed. S. S. Holt, S. G. Neff, & C. M. Urry, (New York: AIP), 486

Antonucci, R. R. J., Geller, R., Goodrich, R. W., Miller, J. S. 1996, *ApJ*, in press

Antonucci, R. R. J., Kinney, A. L., & Ford, H. C. 1989, *ApJ*, 342, 64

Bahcall, J. N., et al. 1993, *ApJS*, 87, 1

Baldwin, J. A. 1977a, in *Active Galactic Nuclei*, ed. C. Hazard & S. Mitton, (Cambridge: Cambridge Univ. Press), 51

_____. 1977b, *ApJ*, 214, 679

Blaes, O., & Agol, E. 1996, *ApJ*, in press

Boyle, B. J. 1990, *MNRAS*, 243, 231

Burstein, D., & Heiles, C. 1978, *ApJ*, 225, 40

Christiani, S., & Vio, R. 1990, *A&A*, 227, 385

Czerny, B., & Zbyszewska, M. 1991, *MNRAS*, 249, 643

Davidsen, A. F., Kriss, G. A., & Zheng, W. 1996a, *Nature*, 380, 47

Davidsen, A. F., Kriss, G. A., Zheng, W., & Bi, H. G. 1996b, in preparation

Davidsen, A. F. et al. 1996c, in preparation

Eastman, R. G., & MacAlpine, G. M. 1985, *ApJ*, 299, 785

Francis, P. J. 1993, *ApJ*, 407, 519

Francis, P. J., Hewett, P. C., Foltz, C. B., Chaffee, F. H., & Weynmann, R. J. 1991, *ApJ*, 373, 465

Hamann, F., Zuo, L., & Tytler, D. 1995, *ApJ*, 444, L69

Heiles, C., & Cleary, M. N. 1979, *Aust. J. Phys. Astrophys. Suppl.*, 47, 1

Hewitt, A., & Burbidge, G. R. 1993, *ApJS*, 87, 451

Hu, E. M., Kim, T.-S., Cowie, L. L., Songaila, A., & Rauch, M. 1995, *AJ*, 110, 1526

Impey, C. D., Malkan, M. A., Webb, W., & Petry, C. G. 1995, *ApJ*, 440, 80

Kolykhalov, D. L., & Sunyaev, R. A. 1984, *Adv. Space Res.*, 3, 249

Koratkar, A., Antonucci, R. R. J., Goodrich, R. W., Bushouse, H., & Kinney, A. L. 1995, *ApJ*, 450, 501

Koratkar, A. P., Kinney, A. L., & Bohlin, R. C. 1992, *ApJ*, 400, 435

Kriss, G. A. 1994, in Astronomical Data Analysis Software and Systems III, A.S.P. Conf. Series, V. 61, ed. D. R. Crabtree, R. J. Hanisch & J. Barnes (San Francisco: Astronomical Society of the Pacific), 437

Krolik, J. H., & Kallman, T. R. 1988, *ApJ*, 324, 714.

Kulkarni, V. P., & Fall, M. 1993, *ApJ*, 413, L63

Laor, A., Bahcall, J. N., Januzzi, B. T., Schneider, D. P., & Green, R. F. 1995, *ApJS*, 99, 1

Laor, A., Bahcall, J. N., Januzzi, B. T., Schneider, D. P., Green, R. F., & Hartig, G. F. 1994, *ApJ*, 420, 110

Laor, A., Netzer, H., Piran, T. 1992, *MNRAS*, 242, 560

Lee, G.-H. 1995, Ph.D. thesis, Johns Hopkins University

Lee, G., Kriss, G. A., & Davidsen, A. F. 1992, in Testing the AGN Paradigm, ed. S. S. Holt, S. G. Neff, & C. M. Urry, (New York: AIP), 159

Malkan, M. A., & Sargent, W. L. W., 1982, *ApJ*, 254, 22

Mathews, W. G., & Ferland G. J. 1987, *ApJ*, 323, 456

Miralda-Escudé, J., & Ostriker, J. P. 1990, *ApJ*, 350, 1

Møller, P., & Jakobsen, P. 1990, *A&A*, 228, 299

Netzer, H., Elitzur, M., & Ferland, G. J. 1985, *ApJ*, 299, 752

O'Brien, P. T. 1987, in Emission Lines in Active Galactic Nuclei, ed. P. M. Gondhalekar, Rutherford Appleton Laboratory: RAL-87-109, 35

O'Brien, P. T., Gondhalekar, P. M., & Wilson, R. 1988, *MNRAS*, 233, 801

Pickard, A., & Jakobsen, P. 1993, *A&A*, 276, 331

Press, W. H., & Rybicki, G. B. 1993, *ApJ*, 418, 585

Schmidt, M. 1963, *Nature*, 197, 1040

Seaton, M. 1979, *MNRAS*, 187, 73P

Shapiro, P. R., Giroux, M. L., & Babul, A. 1994, *ApJ*, 427, 25

Shields, G. 1978, *Nature*, 272, 706

Stark, A. A., Gammie, C. F., Wilson, R. W., Bally, J., Linke, R. H., Heiles, C., & Hurwitz, M. 1992, *ApJS*, 79, 77

Sun, W.-H., Malkan, M. A., & Chang, T. H. W. 1993, *BAAS*, 25, 1432

Turner, T. J., et al. 1993, *ApJ*, 407, 556

Tytler, D., & Davis, C. 1993, *BAAS*, 25, 1432

Véron-Cetty, M.-P., & Véron, P. 1993, A Catalogue of Quasars and Active Nuclei (6th edition), ESO, Garching

Zheng, W., Fang, L. Z., & Binette, L. 1992, ApJ, 392, 74

Zheng, W., et al. 1995, ApJ, 444, 632

_____. 1996, in preparation

FIGURE CAPTIONS

Figure 1. – Redshift distribution of sample quasars, with bin size of 0.33.

Figure 2. – Lyman valley correction curves as a function of redshift for lines with neutral–hydrogen column density between 2×10^{12} and 10^{16} cm $^{-2}$.

Figure 3. – Number of merging spectra as function of rest–frame wavelength. Wavelength gaps between merging spectra and the exclusion of pixels with very low S/N level cause narrow features at short wavelengths.

Figure 4. – Signal–to–noise level per Å as function of rest–frame wavelength. The actual level may be slightly lower due to uncertainties in the FOS flat–field corrections. Correlated errors between adjacent re–binned pixels are not taken into account.

Figure 5. – Composite FOS spectrum of 101 quasars, binned to 2 Å. Prominent emission lines and the Lyman limit are labeled, and two possible emission features are marked. The continuum fitting windows are marked with the bars near the bottom.

Figure 6. – Root–mean–square deviation per merging spectrum normalized as a fraction of the composite spectrum in Fig. 5.

Figure 7. – Spectral region near the Lyman limit. The spectrum is the same as Fig. 5, but displayed with 0.3 Å bins. The dotted line represents the broken power-law continuum fitted in other windows (see §3.1). The contributions to χ^2 for each bin relative to the fitted continuum are plotted in the lower panel.

Figure 8. – Composite FOS spectra of 60 radio–loud and 41 radio–quiet quasars, binned to 2 Å. The flux level in the spectrum for radio–quiet quasars is shifted down for display purposes. Prominent emission lines and the Lyman limit are marked.

Figure 9. – Comparison of quasar composite spectra. Solid curve: composite FOS spectrum of radio–quiet quasars, representative of $z \approx 1$; dashed curve: optical composite spectrum of Francis et al. (1991), representative of $z \approx 3$. The spectra are scaled so that the continuum levels around 1450 Å in both spectra match.

Figure 10. – Model fit of Comptonized accretion disk to the composite FOS spectrum. The composite spectrum is binned to 1 Å and normalized to the mean specific luminosity of the full

sample. The accretion disk model shown is a sum of blackbodies in the Schwarzschild metric for a black hole mass of $1.4 \times 10^9 M_{\odot}$, an accretion rate of $2.8 M_{\odot} \text{ yr}^{-1}$, and a Lyman edge with optical depth 0.8. The disk has an inclination of 30° . The assumed spherical Comptonizing medium has an optical depth of 1.0 and a temperature of $4.1 \times 10^8 \text{ K}$.

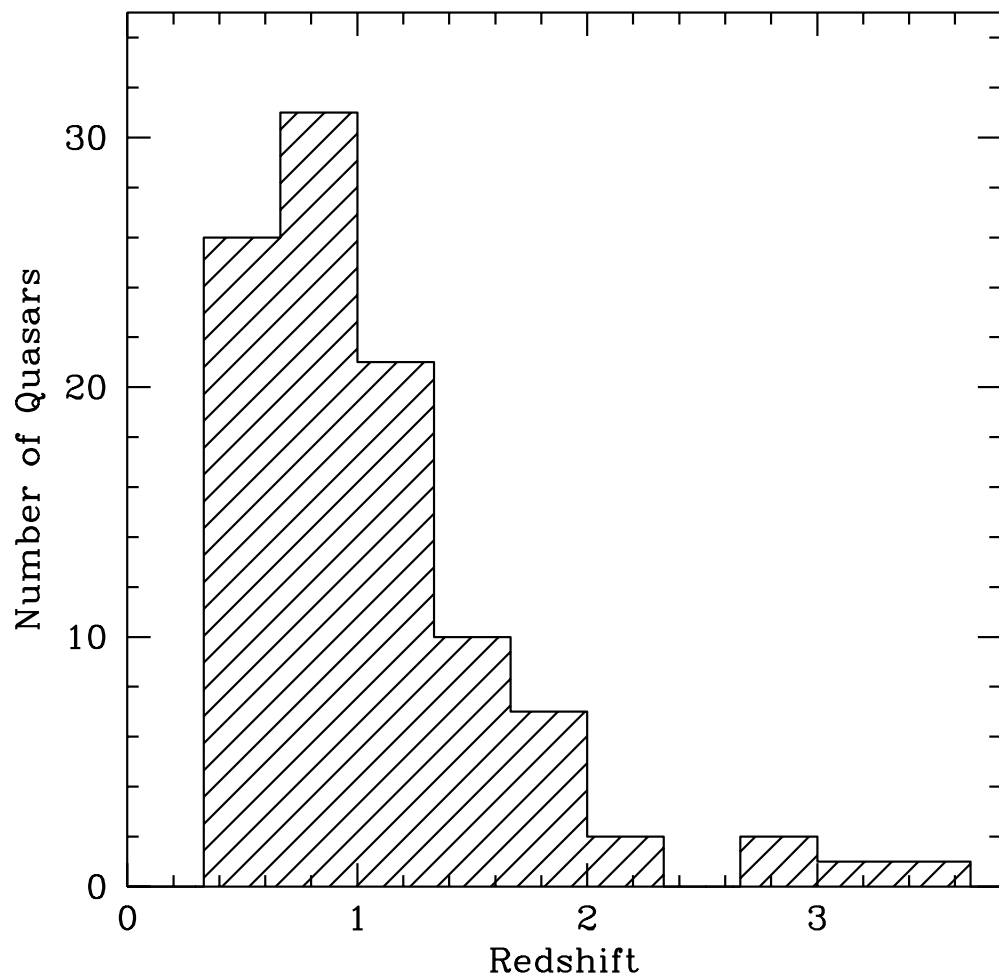


Fig. 1.—

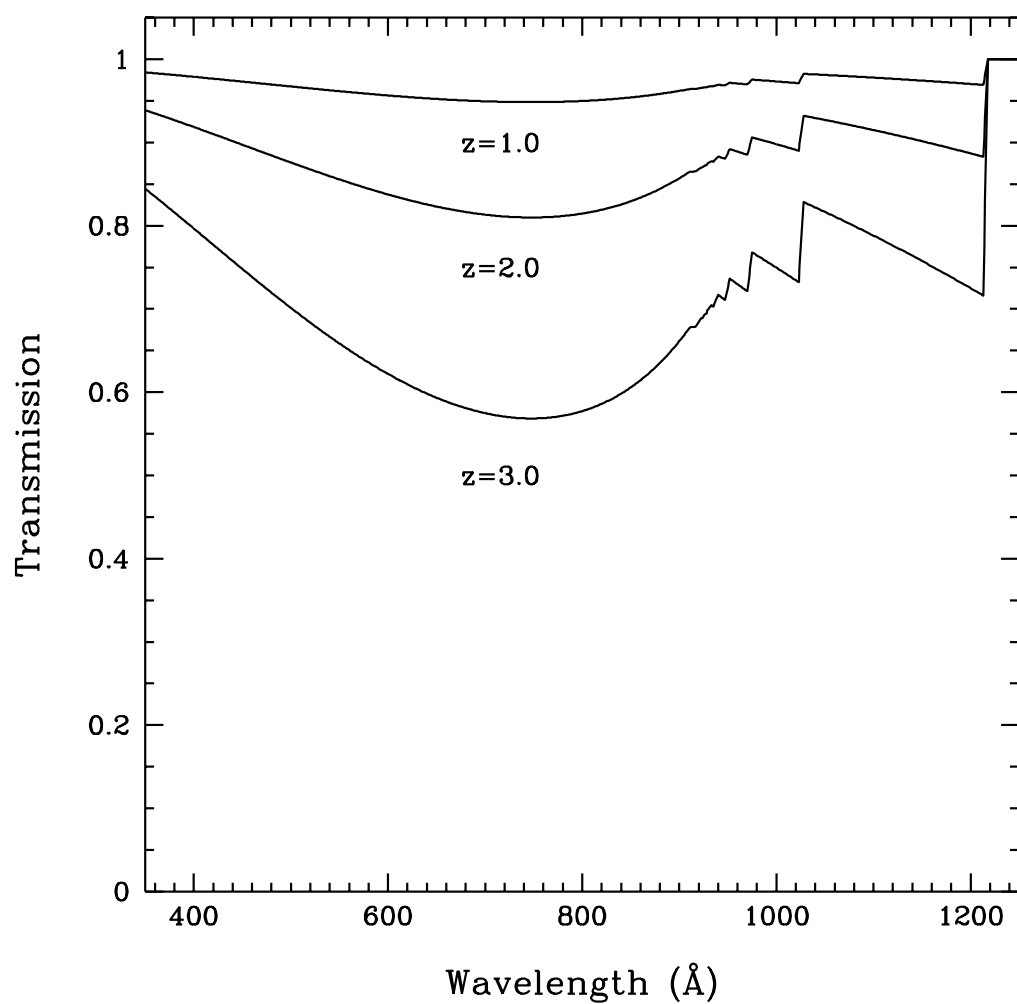


Fig. 2.—

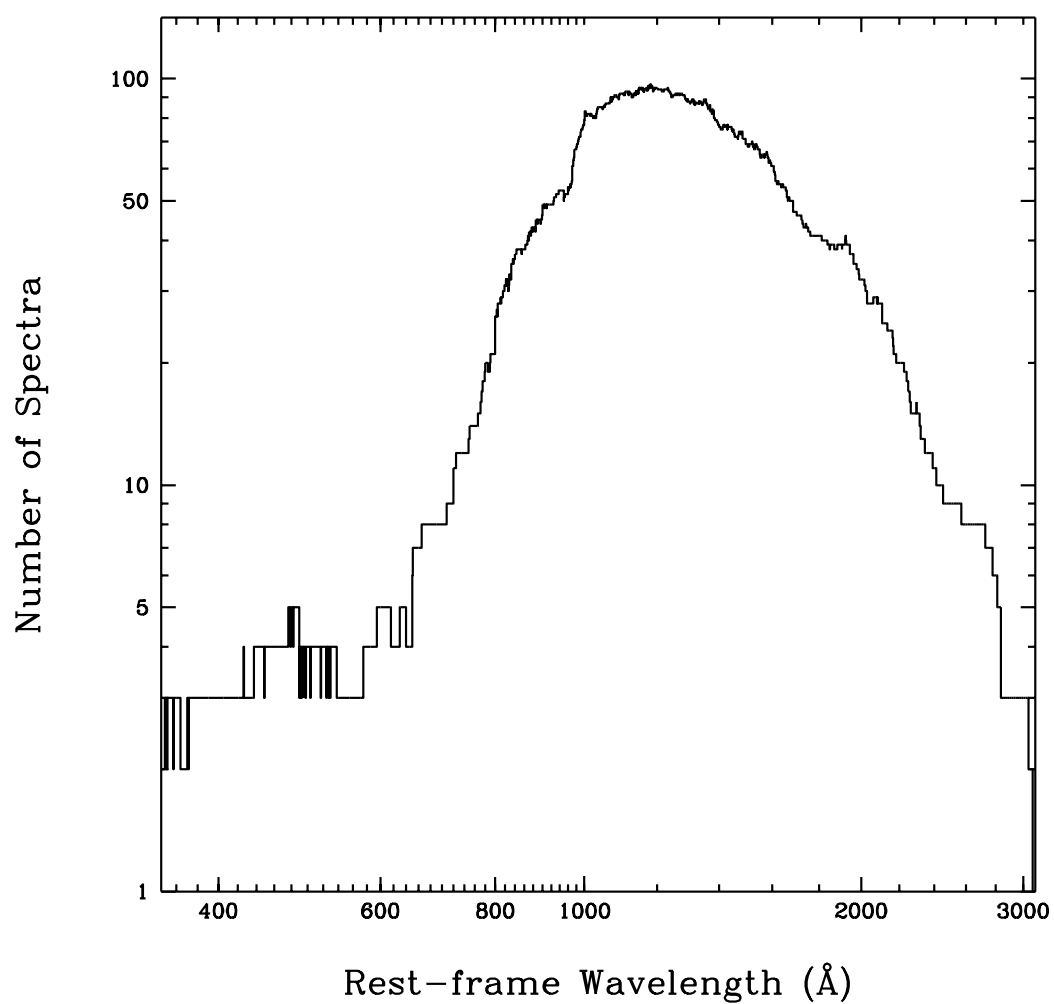


Fig. 3.—

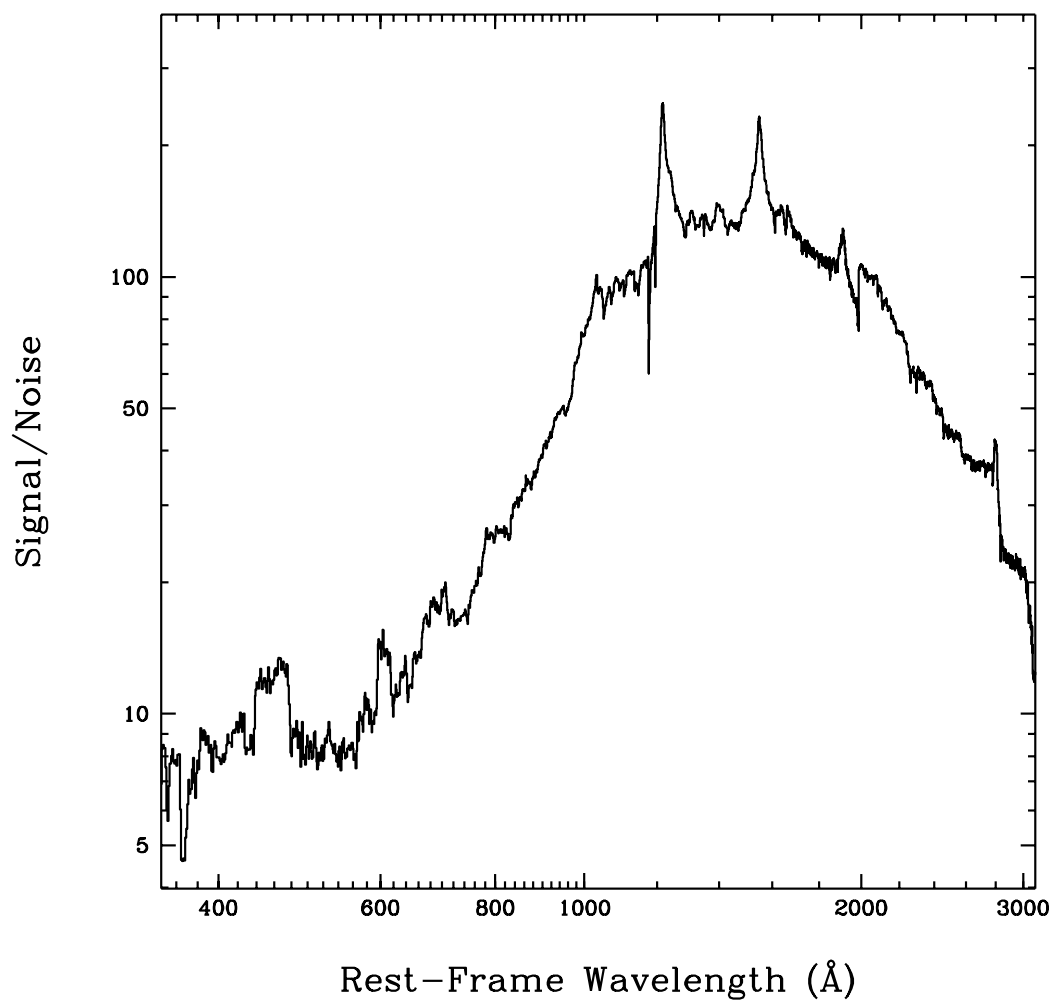


Fig. 4.—

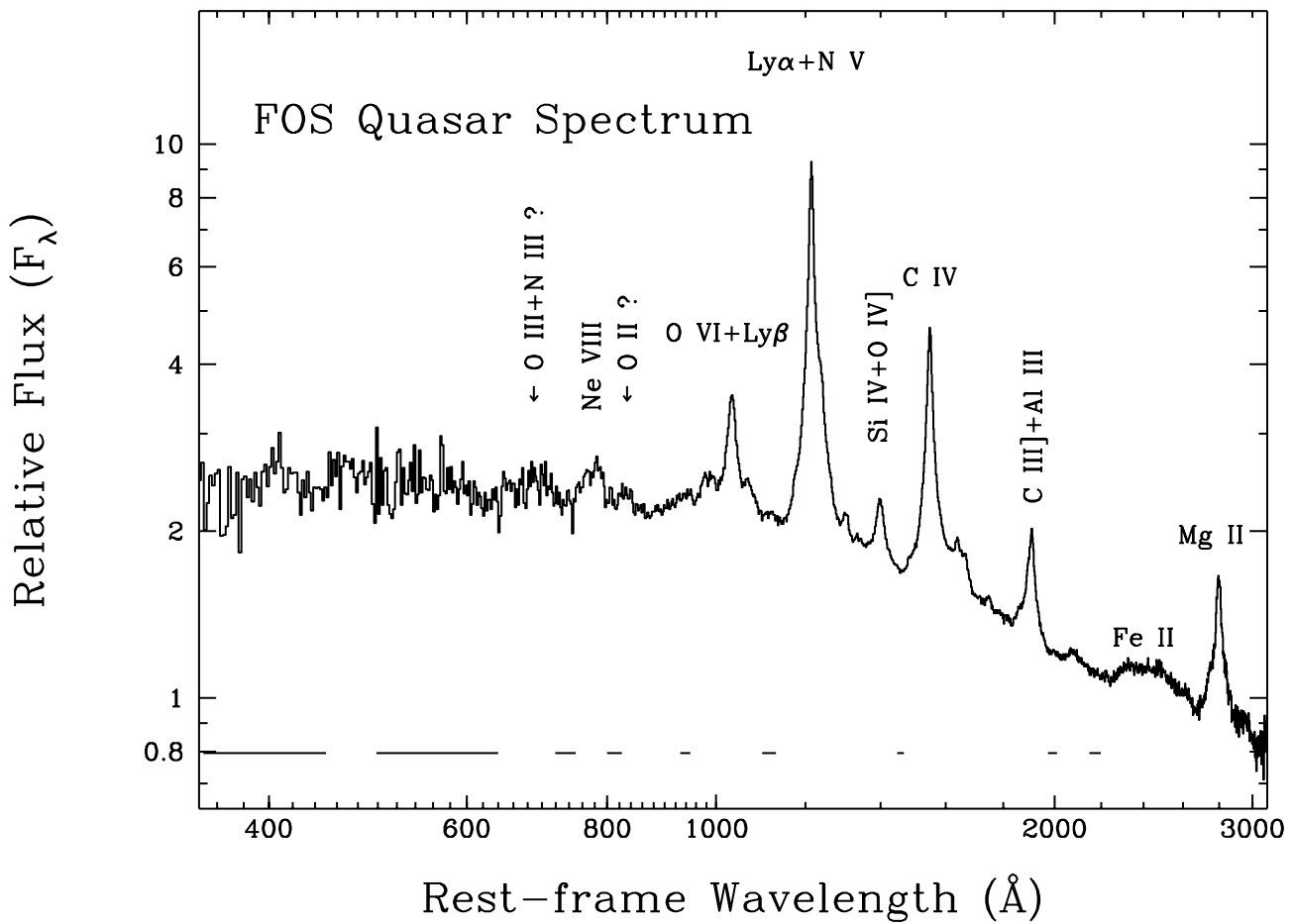


Fig. 5.—

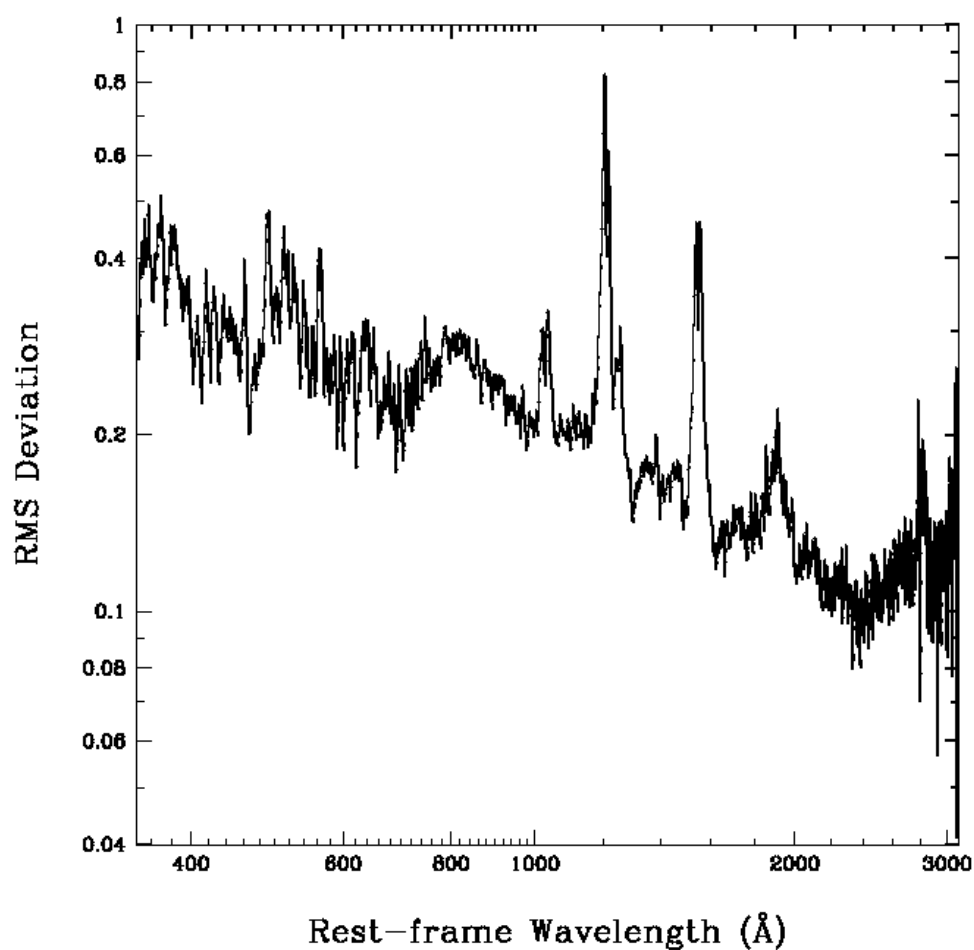


Fig. 6.—

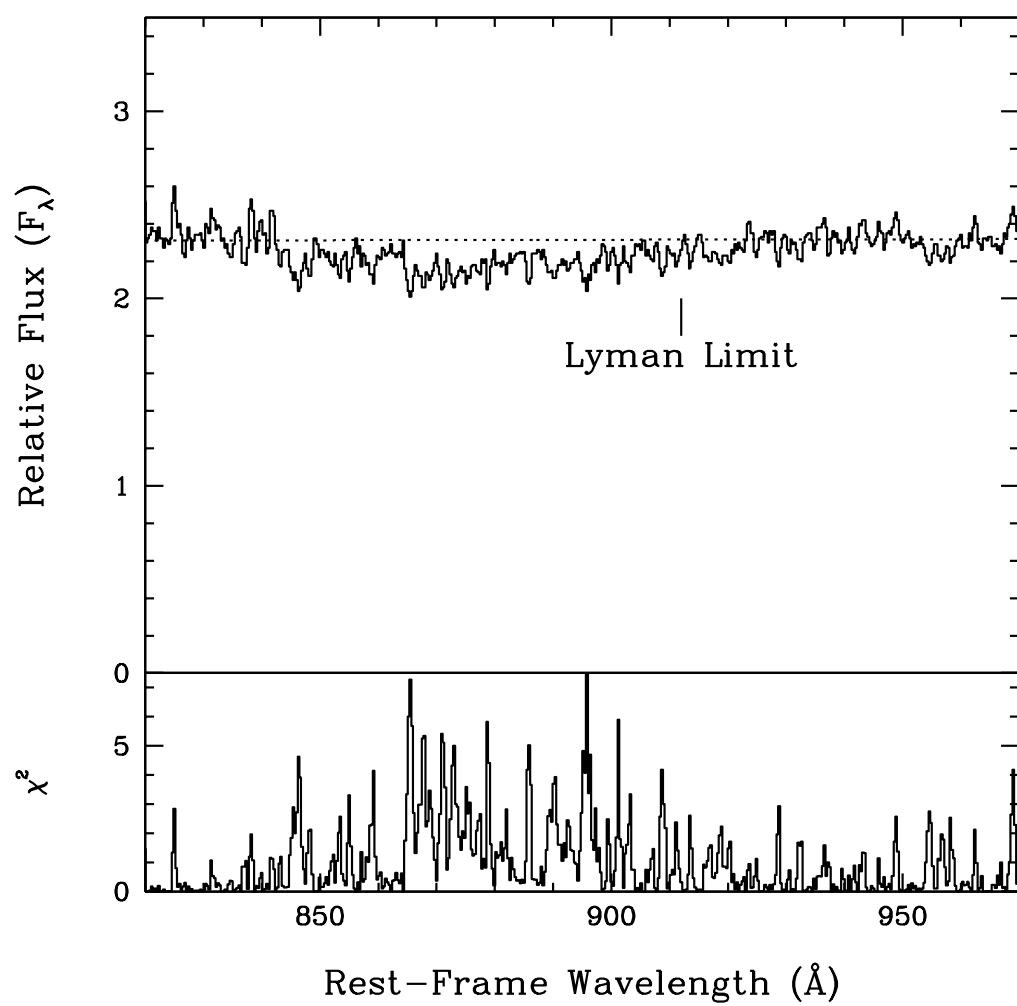


Fig. 7.—

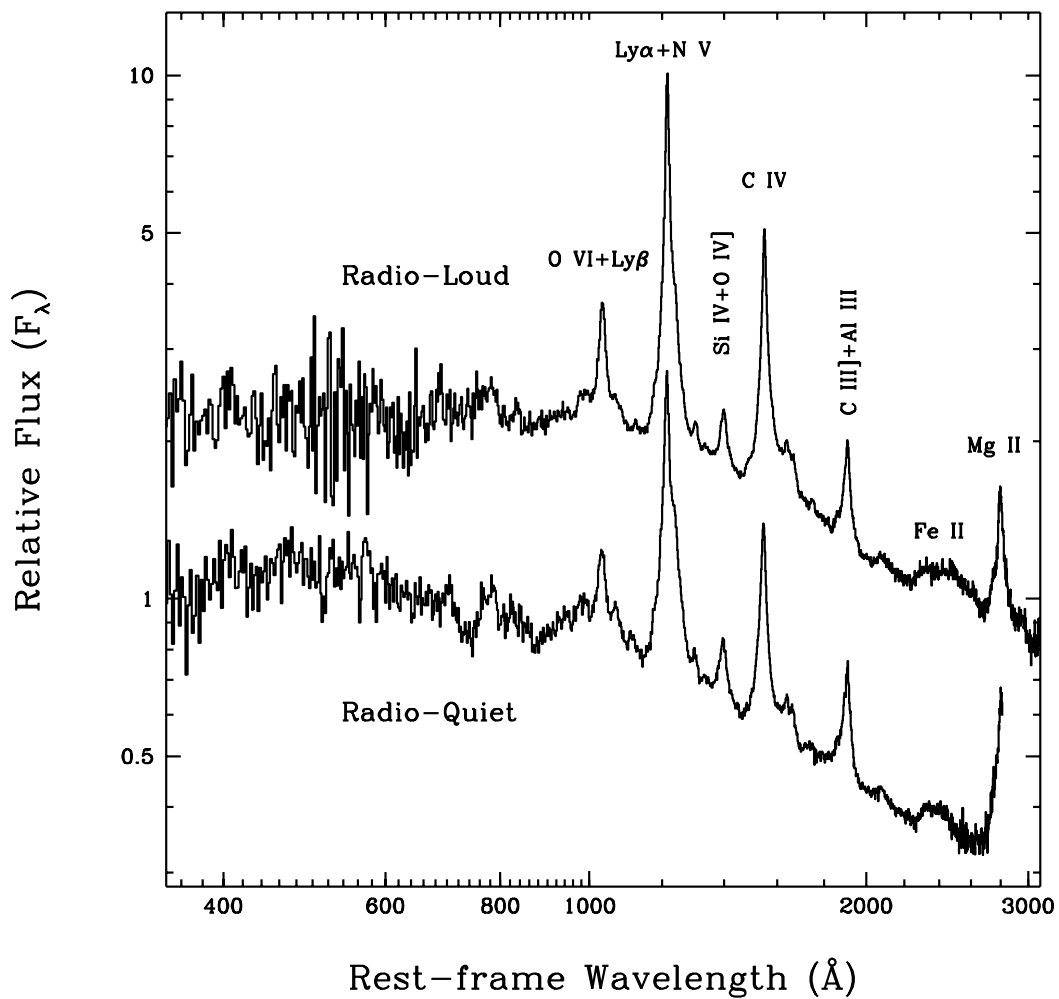


Fig. 8.—

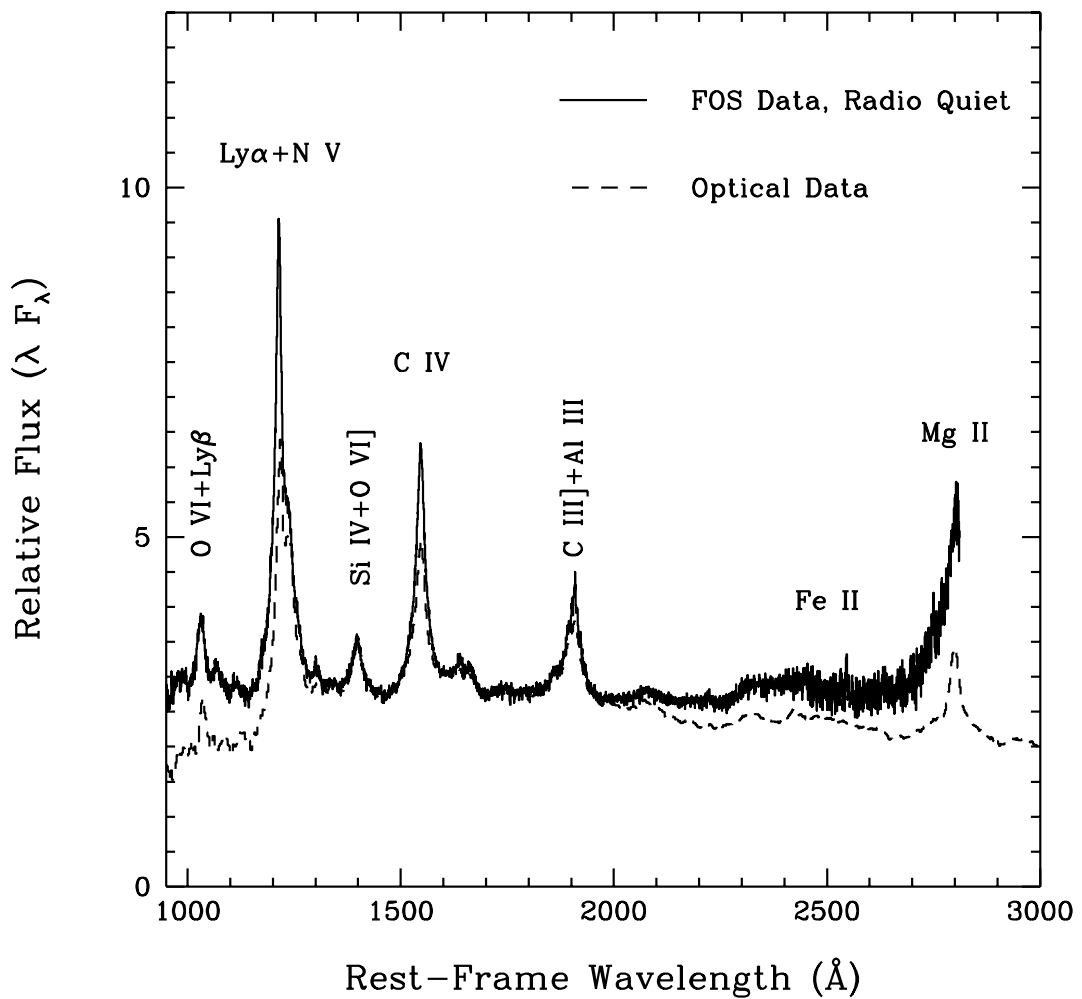


Fig. 9.—

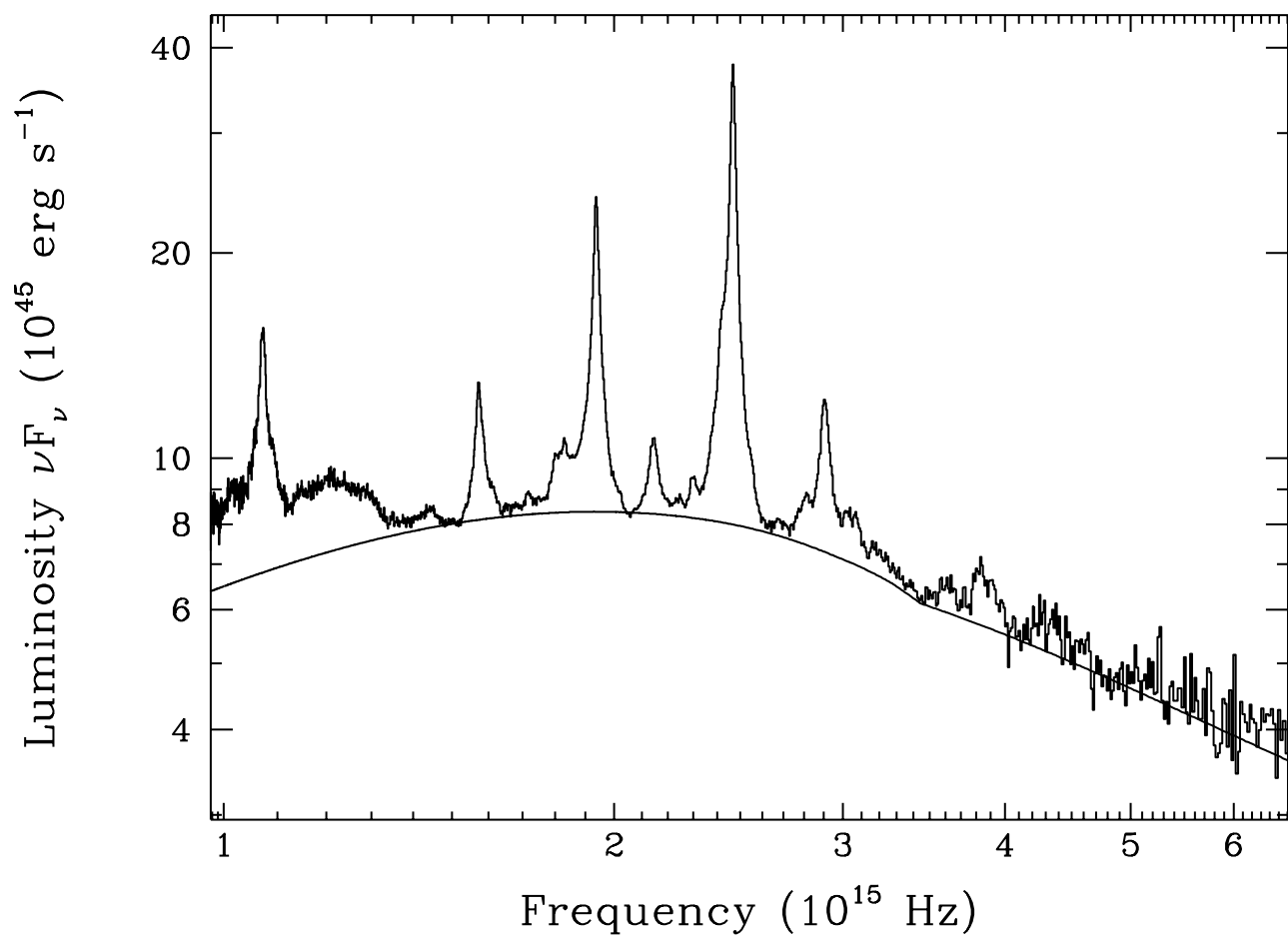


Fig. 10.—